Accepted Manuscript online: 2021-10-27 Article published online: 2021-11-26

Red Thermally Activated Delayed Fluorescence in Dibenzopyridoquinoxaline-Based Nanoaggregates

Subhadeep Das[a]
Subhankar Kundu[a]
Bahadur Sk[a]
Madhurima Sarkar[a]
Abhijit Patra[*a]

[a] Department of Chemistry, Indian Institute of Science Education and Research Bhopal, Bhauri, Bhopal, Madhya Pradesh, 462066, India.

[*] abhijit@iiserb.ac.in

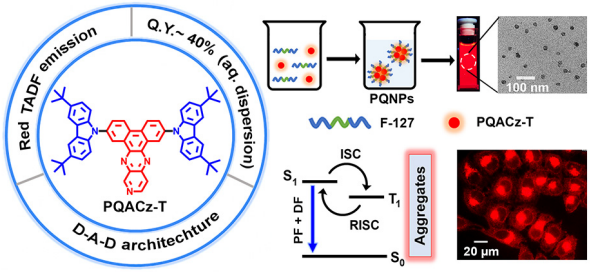

Received: 01.08.2021
Accepted after revision: 26. 10. 2021
DOI: 10.1055/a-1679-9558; Art ID: OM-2021-08-0038-OA

Abstract All-organic thermally activated delayed fluorescence (TADF) materials have emerged as potential candidates for optoelectronic devices and biomedical applications. However, the development of organic TADF probes with strong emission in the longer wavelength region (> 600 nm) remains a challenge. Strong π-conjugated rigid acceptor cores substituted with multiple donor units can be a viable design strategy to obtain red TADF probes. Herein, 3,6-di-*t*-butyl carbazole substituted to a dibenzopyridoquinoxaline acceptor core resulted in a T-shaped donor–acceptor–donor compound, PQACz-T, exhibiting red TADF in polymer-embedded thin-films. Further, PQACz-T self-assembled to molecular nanoaggregates of diverse size and shape in THF–water mixture showing bright red emission along with delayed fluorescence even in an aqueous environment. The self-assembly and the excited-state properties of PQACz-T were compared with the nonalkylated analogue, PQCz-T. The delayed fluorescence in nanoaggregates was attributed to the high rate of reverse intersystem crossing. Moreover, an aqueous dispersion of the smaller-sized, homogeneous distribution of fluorescent nanoparticles was fabricated upon encapsulating PQACz-T in a triblock copolymer, F-127. Cytocompatible polymer-encapsulated PQACz-T nanoparticles with large Stokes shift and excellent photostability were demonstrated for the specific imaging of lipid droplets in HeLa cells.

Key words: TADF, dibenzopyridoquinoxaline, nanoaggregates, fluorescence imaging, lipid droplets

Introduction

All-organic thermally activated delayed fluorescence (TADF) materials have drawn interest recently due to their potential in high-performance organic light-emitting diodes with nearly 100% theoretical internal efficiency.[1–6] Molecules with a small energy gap (ΔE_{ST}) between the lowest energy singlet (S_1) and triplet states (T_1) favour an efficient reverse intersystem crossing (RISC) process.[1,4–9] A small ΔE_{ST} can be obtained by minimizing the overlap between the frontier molecular orbitals, i.e., HOMO and LUMO.[4–12] In this context, various design strategies, including donor–acceptor (D–A) or donor–π–acceptor (D–π–A) architecture, and the introduction of multiple strong donors or acceptor units with twisted molecular structures resulting in significant intramolecular charge transfer (ICT), have been explored.[4,10,12–20] However, as low orbital overlap results in weaker oscillator strength (*f*), achieving simultaneously high photoluminescence (PL) quantum yield and small ΔE_{ST} is challenging.[3] Fine-tuning the orbital overlap by the introduction of rigid or flexible π-spacers has often been used to overcome this issue.[7,21,22]

Recently, efficient blue and green TADF emitters have been developed employing the twisted D–π–A architecture.[22,23] However, optimizing the design strategy to obtain highly efficient red-emitting TADF materials suitable for organic photovoltaics, sensors, or intracellular imaging still remains elusive.[24–28] The dominance of nonradiative deactivations at the higher wavelength according to the energy gap law along with the low oscillator strength due to weak D–A conjugation limits the efficiency of red TADF emitters.[29] Thus, strong π-conjugated rigid acceptor cores are desired to provide deep LUMO levels resulting in low bandgap energy along with suppressed vibrational motions. However,

strong π–π stacking interactions may also quench the fluorescence in the aggregated or solid-state.[30,31]

The quenching of emission can be circumvented by inducing twisted molecular structures or by introducing bulky terminal substituents into the donor/acceptors, thus reducing the π–π stacking in the aggregated state.[32–36] Herein, we developed a T-shaped molecular TADF emitter, PQACz-T, using dibenzo[*f,h*]pyrido[3,4-*b*]quinoxaline (DBPQ) as a rigid acceptor and 3,6-di-*t*-butyl carbazole (DTCz) as a donor. We anticipated that the introduction of bulky *tert*-butyl groups at the 3,6-positions of carbazole would increase the donor strength and might reduce the π–π stacking in the aggregated state. Comparing with the nonalkylated analogue, PQACz-T exhibited enhanced red TADF emission in the aqueous dispersion of nanoaggregates and thin films. Steady-state and time-resolved emission measurements coupled with computational investigations were carried out to elucidate the TADF properties. Furthermore, the amphiphilic triblock copolymer-encapsulated PQACz-T nanoparticles with an average diameter of 20 ± 4 nm were employed for the intracellular imaging of lipid droplets (LDs).

Results and Discussion

The synthetic route of PQACz-T is illustrated in Scheme 1 Friedel–Crafts alkylation of carbazole using *t*-butyl chloride resulted in the donor unit, DTCz (Scheme S1). 2,7-Dibromophenanthrene-9,10-dione (**P2**) was synthesized via the bromination of phenanthrene-9,10-dione (**P1**) using *N*-bromosuccinimide under acidic conditions. The key intermediate compound, 2,7-dibromodibenzo[*f,h*]pyrido[3,4-*b*]quinoxaline (**P3**), was synthesized by the Schiff base condensation between **P2** and 3,4-diaminopyridine. Subsequently, the Pd-catalysed Buchwald–Hartwig coupling between **P3** and DTCz led to the desired product PQACz-T with approximately 65% yield. The nonalkylated analogue, PQCz-T, was synthesized following the protocol developed by our group earlier (Scheme 1).[37] The purity of PQACz-T and all the intermediate compounds was ascertained by ^{1}H-NMR, ^{13}C-NMR spectroscopy, and high-resolution mass spectrometry [Supporting Information (SI) Figures S37–S46].

PQACz-T showed multiple absorption peaks in solvents of varying polarity (Figure 1a, SI, Figure S1, Table S1). The intense absorption bands at ~359 nm (ε ~$2.4 \times 10^4 \cdot M^{-1} \cdot cm^{-1}$) and ~390 nm (ε ~$4.9 \times 10^3 \cdot M^{-1} \cdot cm^{-1}$) were attributed to the π–π* transitions of the donor (DTCz) and acceptor (DBPQ) units, respectively (Figure 1a, SI, Figure S1). The red-shifted broad and weak absorption band (ε ~$1.2 \times 10^3 \cdot M^{-1} \cdot cm^{-1}$) at ~400–550 nm might be due to the ICT from the donors (DTCz) to the acceptor (DBPQ) unit.[18] The optical bandgap of PQACz-T was estimated from the onset of absorption, and it was found to be 2.35 eV (SI, Figure S2).

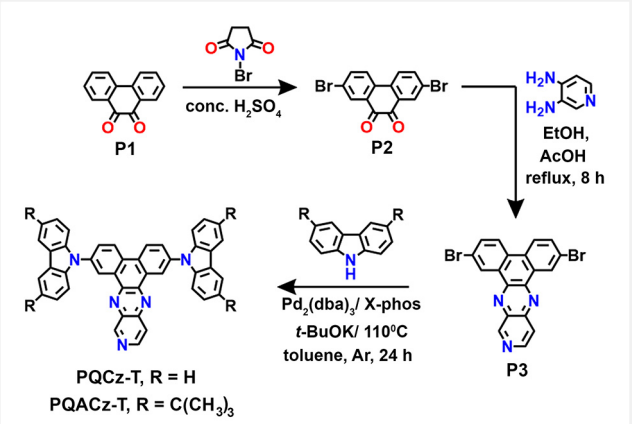

Scheme 1 The synthetic scheme of dibenzopyridoquinoxaline-based T-shaped D–A–D molecules PQCz-T and PQACz-T.

The emission spectra of PQACz-T in solvents of varying polarity revealed a bathochromic shift in emission maxima from 538 nm (hexane; green) to 697 nm (dichloromethane; red, Figure 1b). The full-width at half-maximum (FWHM) also gradually increased from 88 nm (hexane) to 158 nm (dichloromethane). The large positive solvatochromic shift, along with the gradual increase in the FWHM, suggested a typical excited-state ICT character (Figure S4).[18,37–39] The fluorescence quantum yield in toluene was found to be ~37%, which decreased gradually with increasing solvent polarity (< 1% in dichloromethane, SI, Table S2). The red shift and decrease in quantum yields in polar solvents were associated with the enhanced nonradiative transitions and could be due to the twisted ICT (TICT).[37,40,41] The basic spectroscopic properties and the charge transfer characteristics of PQCz-T were reported in our previous study (SI, Figure S5, Table S3).[37] The emission maxima of PQACz-T (λ_{em} = 590 nm, toluene) showed a bathochromic shift as compared to PQCz-T (λ_{em} = 564 nm, toluene) due to the presence of electron-donating alkyl units in the donor DTCz.

The transient PL decay measurements exhibited bi-exponential decay for PQACz-T, which could be due to the existence of locally excited (LE) and charge transfer (CT) states (SI, Figure S6, Table S4).[18] The reconstructed emission spectra of PQACz-T obtained through the time resolved emission spectra (TRES) analysis at 1.1 ns showed a distinct spectral profile resembling the emission spectrum of DTCz in toluene, referring to the LE-state emission (SI, Figure S7). However, the steady-state emission spectrum was significantly red-shifted and originated from the CT state. A broad emission spectrum with a peak maximum at 608 nm was observed for PQACz-T in toluene at 77 K (SI, Figure S8). TRES measurements were carried out in toluene at room temperature and 77 K to obtain the energy difference between the singlet and triplet states (Figure 1c). The S_1 and T_1 energy

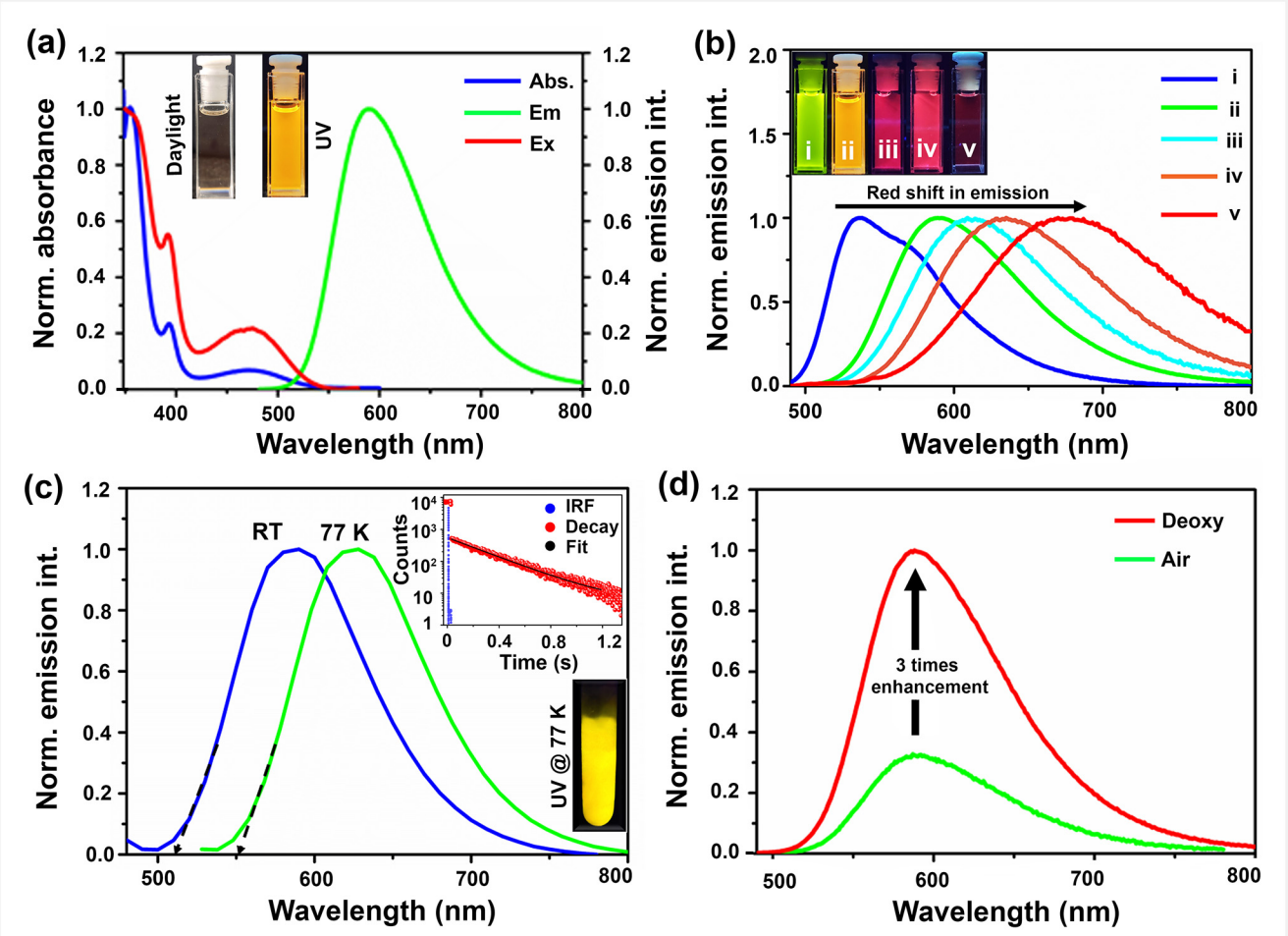

Figure 1 (a) Normalized absorption, emission, and excitation spectra of PQACz-T in toluene under ambient conditions; inset: digital photographs of PQACz-T in toluene under daylight and UV irradiation (λ_{ex} = 365 nm). (b) Normalized emission spectra of PQACz-T in (i) hexane, (ii) toluene, (iii) dioxane, (iv) tetrahydrofuran, and (v) dichloromethane; inset: digital photographs depicting the solvatochromic shift in the emission spectra with increasing solvent polarity under UV lamp illumination (λ_{ex} = 365 nm). (c) Time-resolved emission spectra (TRES) of PQACz-T in toluene at room temperature (time delay: 10 ns, blue) and liq. N_2 temperature (77 K, time delay: 280 ms, green). The inset figures depict the transient PL decay of PQACz-T at 77 K and the digital photograph showing phosphorescence at 77 K under UV irradiation. (d) Emission spectra of PQACz-T in toluene at room temperature under air (green) and after deoxygenation with prolonged N_2 purging (red). For (a–d), the concentration of PQACz-T was kept constant at 10 µM, λ_{ex} = 470 nm.

levels were estimated from the onset of fluorescence (room temperature measurement, time delay: 10 ns) and phosphorescence (77 K measurement, time delay: 280 ms) spectra and were found to be ~2.44 and 2.24 eV, respectively, resulting in a ΔE_{ST} of 0.20 eV (Figure 1c).

A three-times enhancement in the emission intensity of PQACz-T in toluene was noticeable upon deoxygenation with prolonged nitrogen-purging, indicating the possibility of fluorescence quenching by molecular oxygen (Figure 1d).[42,43] Moreover, upon deoxygenation, a long-lived emission was observed in the microsecond time domain (τ_{avg} = 4.5 µs, Figure 2a, SI, Table S5). TRES measurements at room temperature revealed that the decay-associated emission spectra at the microsecond (time delay: 4.5 µs) and nanosecond (time delay: 10 ns) timescales were identical, indicating the delayed fluorescence phenomenon in PQACz-T (Figure 2b). The activation energy of RISC for PQACz-T in toluene was found to be 0.14 ± 0.03 eV, very close to the ΔE_{ST} value (Figure 2c, SI, Table S6).[1] Furthermore, the laser power-dependent emission study was performed to assign the nature of the delayed fluorescence.[7,12,18] The linear dependence of the delayed fluorescence intensity as a function of laser power, with a slope of 1.04, confirmed the TADF process over the triplet–triplet annihilation (Figure 2d).[7,12,18]

Density-functional theory (DFT) and time-dependent DFT (TDDFT) calculations at the B3LYP/6-31G(d,p) level revealed the ground state geometry and the excited-state

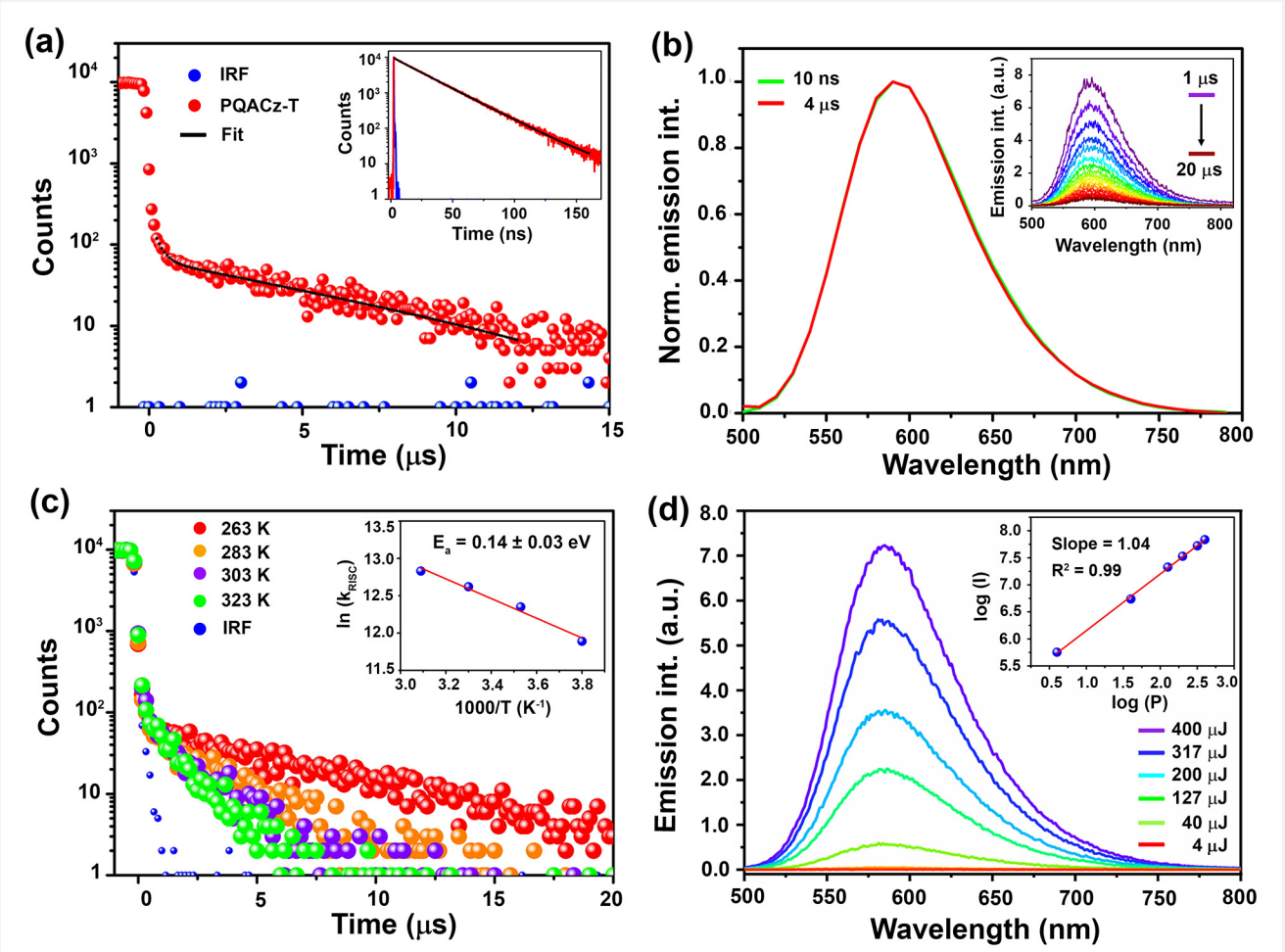

Figure 2 (a) Transient photoluminescence (PL) decay of PQACz-T in deoxygenated toluene at microsecond timescale at room temperature; inset: transient PL decay of PQACz-T in deoxygenated toluene at the nanosecond timescale at room temperature. (b) Time-resolved emission spectra (TRES) of PQACz-T in deoxygenated toluene at room temperature at microsecond (time delay: 4 μs, red) and nanosecond timescale (time delay: 10 ns, green), ascertaining delayed fluorescence. The inset figure depicts the TRES analysis of PQACz-T in deoxygenated toluene recorded with an intensified charge-coupled device (iCCD) camera with a tunable excitation source using optical parametric oscillator (OPO) crystal. (c) Temperature-dependent transient decay spectra of PQACz-T in deoxygenated toluene; inset: the Arrhenius plot of activation energy (E_a) for the reverse intersystem crossing (RISC). (d) Laser power-dependent emission spectra of PQACz-T in deoxygenated toluene under ambient conditions; inset: linear fitting of the emission intensity of PQACz-T as a function of excitation power. λ_{ex} = 470 nm, conc: 10 μM.

electronic distributions of the molecule, respectively. The dihedral angle between the donor (DTCz) and acceptor (DBPQ) units was found to be ~50° in the ground-state optimized structure (SI, Figure S10). As shown in Figure 3a, the LUMO (−2.77 eV) was predominantly localized on the central acceptor core, while the HOMO (−5.17 eV) was located on both the donor units. The computed energy gap was found to be ~2.4 eV, corroborated well to the optical band gap (~2.35 eV, SI, Figure S2). The TDDFT calculations suggested a low ΔE_{ST} value of 0.18 eV, similar to that obtained from the experimental results, indicating the possible facile intersystem crossing (ISC)/RISC pathways (Figure 3b, SI, Table S7).

The cyclic voltammogram of PQACz-T indicated one quasi-reversible oxidation reaction and two quasi-reversible reduction reactions (Figure 3c). The presence of *t*-butyl groups at the 3,6-positions of the donor unit (DTCz) restricted the oxidative coupling reaction upon electro-oxidation, indicating the electrochemical stability of PQACz-T.[44] The half-wave oxidation and reduction potentials ($E_{1/2}$) were used to calculate the HOMO and LUMO energy levels following the equations (1) and (2).[45]

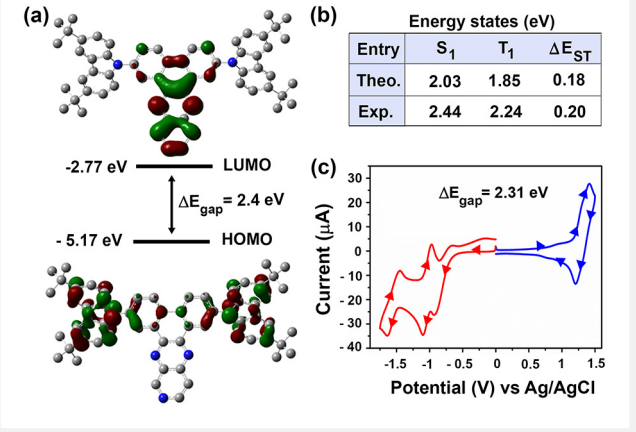

Figure 3 (a) The optimized frontier molecular orbitals (HOMO and LUMO) geometry and the respective energy levels of PQACz-T calculated through density-functional theory (DFT) at the B3LYP/6-31G (d,p) level. (b) Table representing the lowest energy excited singlet (S_1), triplet (T_1) states, and the energy gap (ΔE_{ST}) obtained from the theoretical (Theo.) calculation using time-dependent density functional theory (TDDFT) and experimental (Exp.) measurements at 77 K. (c) Cyclic voltammogram (scan rate: 100 mV/s) of 1 mM solution of PQACz-T in dry dichloromethane using 0.1 M tetrabutylammonium hexafluorophosphate (TBAP) as the supporting electrolyte and glassy carbon as the working electrode. The anodic and cathodic scans are shown in blue and red, respectively. The arrows indicate the direction of the initial scan.

$$E_{HOMO} = -E_{\frac{1}{2}(ox)} - 4.8 + E_{\frac{1}{2}(Fc/Fc^+)} \quad (1)$$

$$E_{LUMO} = -E_{\frac{1}{2}(red)} - 4.8 + E_{\frac{1}{2}(Fc/Fc^+)} \quad (2)$$

The estimated HOMO and LUMO energy levels of PQACz-T were −5.58 and −3.27 eV, respectively, suggesting an electrochemical bandgap of 2.31 eV, which closely resembled the theoretically calculated and experimentally obtained optical band gap (SI, Table S8). Half-wave oxidation potential decreased from PQCz-T to PQACz-T due to the increased donor strength (SI, Figure S11, Table S8).

We investigated the TADF property of PQACz-T in 10 wt% poly(methyl methacrylate) (PMMA) film. Also, the solid film of the compound was fabricated by drop-casting the methanol dispersion onto a quartz plate and followed by drying under vacuum. The emission maximum of the drop-casted film (615 nm) was red-shifted as compared to the PMMA-doped film (565 nm, SI, Figure S12). The red shift in the emission maximum in the solid film might be due to the larger dipole–dipole interactions between the surrounding molecules than in the doped polymer film.[46] The transient PL decay analysis of the PMMA film showed an average prompt and long-lived decay time of 28 ns and 56 µs, respectively (SI, Figure S12, Table S9). TRES measurements of the PMMA film at room temperature signified that the emission spectrum obtained at the microsecond timescale was identical with the nanosecond timescale spectrum (SI, Figure S13). Furthermore, the laser power-dependent study signified a linear relationship between emission intensity and laser power, thereby confirming the TADF property of the PQACz-T-embedded PMMA film (SI, Figure S14). The transient decay measurements (average prompt and delayed decay time of 15 ns and 10 µs, respectively) and TRES analysis of the drop-casted film showed similar observations ascertaining the delayed fluorescence property (SI, Figure S15). The transient decay measurements and TRES analysis of 10 wt% PMMA doped film of PQCz-T also revealed the delayed fluorescence emission (λ_{em} = 540 nm, $\tau_{DF(avg)}$ = 58 µs, SI, Figures S12, S13, Table S9).

The temperature-dependent emission properties of PQACz-T and PQCz-T doped films in PMMA were investigated. The PL intensity was gradually enhanced with increasing temperature (273–313 K) for both PQACz-T- and PQCz-T-doped PMMA films (SI, Figures S16, S17). The average decay times of the delayed component decreased for PQACz-T (96 µs at 273 K to 37 µs at 313 K) and PQCz-T (104 µs at 273 K to 39 µs at 313 K) with the gradual increase of temperature (SI, Figures S16, S17, Table S10). The shorter decay time at higher temperatures could be attributed to the facile RISC involving $T_1 \rightarrow S_1$. However, reverse internal conversion from the $T_1 \rightarrow T_n$ followed by $T_n \rightarrow S_1$ cannot be ruled out in the doped polymer film.[47–49]

The molecules exhibiting TADF emission in the amorphous aggregated state or in the aqueous dispersions are limited compared to those observed in the solid-state or polymer matrices.[25,50,51] The effect of aggregation on the emission and decay properties of PQACz-T and PQCz-T was thus checked in tetrahydrofuran (THF)–water binary solvent mixtures with varying water fractions (f_w, Figure 4, SI, Figures S18, S19). The emission spectra (λ_{em} = 680 nm) showed a bathochromic shift with a reduced emission intensity compared to that of the THF solution when the water fraction was less than 30% for PQACz-T (Figure 4b, SI, Figure S18). At a lower water fraction ($f_w \leq 30\%$), the enhanced polarity of the solvent mixture might result in a dark TICT state, causing the bathochromic shift with quenched emission as evident from the solvatochromic experiments (Figure 1b, SI, Figure S4).[18,37,52] The fluorescence intensity thereafter increased, though it was lower than that of the THF solution till $f_w \leq 50\%$. The plot of the extent of aggregation against the water fractions revealed a steep rise at 70–80% water fraction, indicating it as the most significant regime of aggregation for PQACz-T (SI, Figure S20). The maximum emission intensity was observed at f_w = 99%, with λ_{em} = 623 nm, slightly blue-shifted than that of the THF solution (λ_{em} = 632 nm). The formation of aggregates impeded the intramolecular motions and nonradiative relaxations, which contributed to a reduction of Stokes shift leading to a blue shift along with a 3-fold rise in the emission intensity of

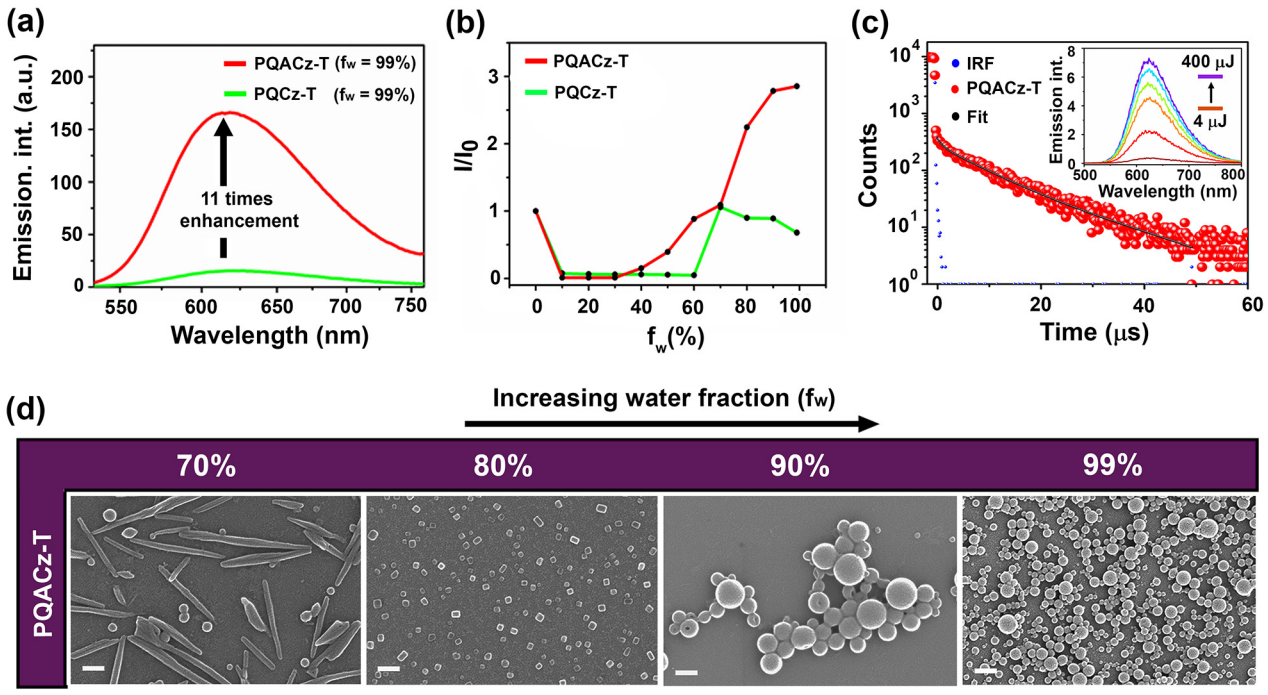

Figure 4 Photophysical and morphological properties of the nanoparticles of PQACz-T and PQCz-T formed in THF–water binary solvent mixture: (a) emission spectra of the nanoparticles of PQACz-T and PQCz-T in 99% water fraction at room temperature; (b) intensity ratio versus the fraction of water plot for the nanoparticles of PQACz-T and PQCz-T, where I_0 denotes the intensity at the emission maxima of the pristine molecule in THF, and I denotes the intensity at the emission maxima of different nanoparticles; (c) transient PL decay curves at the microsecond timescale showing the long-lived emission of PQACz-T nanoparticles formed in 99% water fraction at room temperature under ambient conditions; the inset depicts the laser power-dependent emission profile of PQACz-T nanoaggregates (f_w = 99%); (d) field emission scanning electron microscopy (FESEM) images of the nanoparticles of PQACz-T formed in different water fractions; scale = 200 nm.

the nanoaggregates (99% water) compared to that of the THF solution (Figure 4b).[52]

The emission properties of PQCz-T were also monitored under similar conditions. However, no significant enhancement in the fluorescence intensity was observed for the aggregates (Figure 4b, SI, Figure S19). The plot of the extent of aggregation indicated a steep rise in between 60% and 70% water fraction, suggesting it as the most prominent aggregation regime (SI, Figure S20). However, a steady decrease in fluorescence intensity was observed for PQCz-T aggregates beyond 70% water fractions (Figure 4b). The strong π–π interactions might reduce the emission of PQCz-T in the aggregated state due to nonradiative energy transfer.[34,35] In contrast, the presence of bulky *t*-butyl groups in PQACz-T could circumvent the π–π interactions in the aggregated state, leading to fluorescence enhancement.[34,35]

Transient decay measurements were performed with the aggregates at nano- and microsecond timescales (Figure 4c, SI, Figures S21–23, Tables S11–13). Interestingly, the aggregates of PQACz-T formed at or above 50% THF–water solvent mixtures showed a microsecond decay (τ_{avg} = 9 μs, f_w = 99%) along with a prompt nanosecond decay (τ_{avg} = 29 ns, f_w = 99%). Furthermore, the TRES measurements, along with the laser power-dependent study of the nanoaggregates (f_w = 99%), confirmed the TADF property (Figure 4c, SI, Figures S24, S25). The prominent delayed fluorescence emission (τ_{avg} = 7 μs) for PQCz-T aggregates was observed only in f_w = 99% water fraction (SI, Figures S23, S26).

Previous reports indicated the enhanced rate of RISC leading to delayed fluorescence in molecular aggregates.[53] We observed a gradual increase in the rate of RISC from 3.2×10^5 to 16.7×10^5 s^{-1} for PQACz-T aggregates with increasing water fraction from 50% to 99%, respectively (Figure 5, SI, Table S14). The enhanced rate of RISC could be attributed to the lowering of ΔE_{ST} in the nanoaggregates at higher water fractions facilitating the delayed fluorescence (SI, Figure S27, Table S15). Similar results of low ΔE_{ST} values in the nanoaggregates of difluoroboron *β*-diketonate-based nanoparticles were demonstrated by Yang and co-workers.[54] The perturbation of the electronic states due to the intermolecular interactions in nanoaggregates results in the reduction of ΔE_{ST}.[53,54] The rate of RISC in PQCz-T nanoaggregates at 99% water fraction was found to be 5.5×10^5 s^{-1} (SI, Table S14).

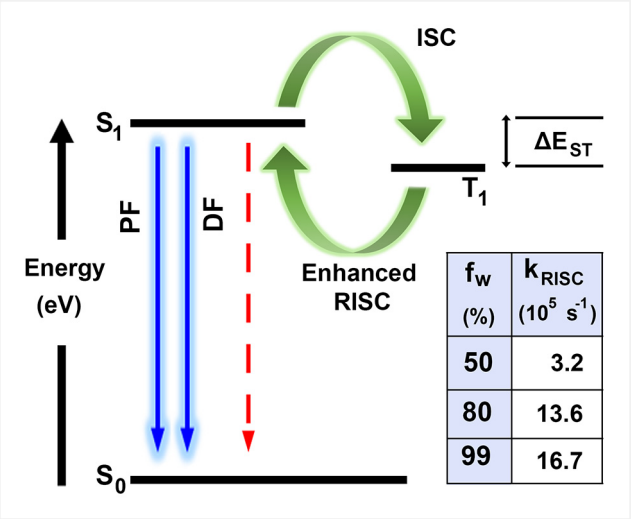

Figure 5 Representative TADF mechanism in PQACz-T nanoparticles. The prompt (PF) and delayed fluorescence (DF) were enhanced with increased water fraction due to the reduction of nonradiative (red) pathways as well as enhancement in intersystem and reverse intersystem crossing (ISC/RISC) rates. The table indicates the enhancement in the rate of RISC values with increasing water fraction (*fw*).

The self-assembly of PQACz-T and PQCz-T towards nanoaggregate formation was probed through field-emission scanning electron microscopy (FESEM) of the drop-casted dispersions. FESEM images of PQACz-T indicated distinct morphologies of the nanoaggregates formed in different water fractions (Figure 4d). The rod-shaped particles were observed at $f_w = 70\%$, and more spherical particles were formed with increasing water fractions. The average diameter of the spherical nanoaggregates formed at 99% water fraction was found to be 110 ± 30 nm. In contrast, only block-shaped particles were formed for PQCz-T under similar conditions (SI, Figure S28). The bulky alkyl chains present in PQACz-T favoured hydrophobic interactions in an aqueous medium resulting in the diverse-shaped aggregate formation.[55,56]

The aqueous dispersion of strongly fluorescent organic nanoparticles (diameter typically < 100 nm) has been explored as potential imaging agents.[25,49,57] However, as mentioned earlier, PQACz-T nanoaggregates fabricated at different compositions of THF–water mixture revealed a broad distribution of particles of diverse sizes and shapes. The molecular self-assembly can be tuned employing amphiphilic surfactants or polymeric micelles through hydrophobic–hydrophobic interactions.[58,59] Herein, we used Pluronic F-127, a neutral triblock copolymer, to encapsulate PQACz-T in water (Figure 6a). The polymer-encapsulated nanoparticles were prepared from the chloroform solution of PQACz-T and F-127 through slow evaporation of the organic solvent followed by dispersing into water.[60] The transmission electron microscopy (TEM) images revealed the spherical morphology of F-127-encapsulated PQACz-T nanoparticles (abbreviated as PQNPs, Figure 6b). The average diameter of PQNPs was found to be much smaller (20 ± 4 nm) with a nearly homogeneous particle size distribution as compared to that of PQACz-T nanoaggregates (110 ± 30 nm for $f_w = 99\%$; Figure 6b, SI, Figure S29).

The aqueous dispersion of PQNPs could be used for non-invasive cellular imaging. The particle size and distribution of PQNPs in aqueous dispersion rather than the solvent-evaporated state as obtained through TEM would be more relevant for imaging. Hence, to obtain the size of the nanoparticles in the dispersion state, the fluorescence correlation spectroscopy (FCS) analysis was carried out for PQNPs and compared with PQACz-T nanoaggregates ($f_w = 99\%$; Figure 6c). A three-dimensional (3D) diffusion model was used to fit the raw FCS traces; (Eqn. 3)[57,61]:

$$G_{3D}(\tau) = \frac{1}{N}\frac{1}{\left(1+\frac{\tau}{\tau_D}\right)}\frac{1}{\sqrt{1+\frac{\tau}{\omega^2\tau_D}}} \quad (3)$$

$G_{3D}(\tau)$ and N are the autocorrelation function and the average number of particles present in the confocal detection volume, respectively. The structural parameter of the 3D Gaussian confocal volume, ω, is defined through its longitudinal (ω_z) and transverse radius (ω_{xy}), as $\omega = \omega_z/\omega_{xy}$. The diffusion time ($\tau_D$) and diffusion constant (D_t) of PQNPs were found to be 2.5 ms and 7.3 $\mu m^2 \cdot s^{-1}$, respectively (Figure 6c, SI, Figure S30, Table S16). On the other hand, the D_t value for PQACz-T nanoaggregates ($f_w = 99\%$) was decreased to 3.9 $\mu m^2 \cdot s^{-1}$ (Figure 6c, SI, Figure S30, Table S16). The hydrodynamic radius of the PQNPs and PQACZ-T aggregates in the dispersion state was calculated using the Stokes–Einstein equation (SI, Eqn. S18). The results revealed a much smaller diameter of PQNPs (58 ± 2 nm) as compared to that of PQACz-T aggregates (110 ± 10 nm) in the aqueous dispersion (SI, Table S16).

The absorption spectrum of PQNPs in water was found to be quite similar to that of PQACz-T in the solution state (Figure 6d). The emission of PQNPs was found to show a peak at 628 nm with an appreciable quantum yield of ~20 ± 0.3%. The transient decay measurements and TRES analysis along with laser power-dependent study confirmed the TADF in PQNPs (Figure 6e, f, SI, Figure S31). The average prompt and delayed decay times were found to be 26 ns and 23 µs, respectively (Figure 6e, Table S17). The smaller particle size, water dispersibility, longer emission wavelength, high quantum yield, and excellent photostability prompted us to check the subcellular internalization of PQNPs (SI, Figure S32).

In order to evaluate the cytocompatibility, MTT assays were carried out using HeLa cells. PQNPs showed low toxicity despite incubating the cells with high concentrations of up to 150 µg/mL (SI, Figure S33). Hence, HeLa cells were in-

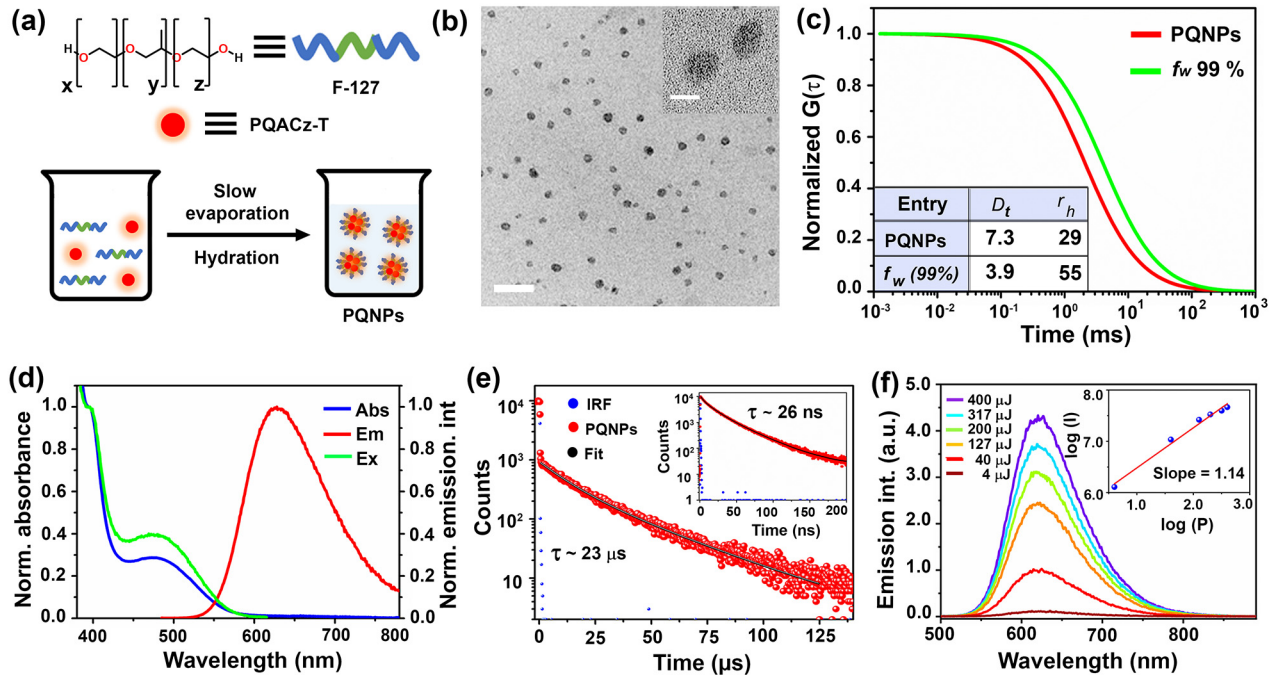

Figure 6 (a) Schematic representation depicting the preparation of aqueous dispersion of PQNP nanoprobe employing Pluronic F-127 triblock copolymer. (b) Transmission electron microscopy (TEM) images of PQNPs (scale = 100 nm); inset: zoomed view of PQNPs (scale = 20 nm). (c) Normalized fluorescence correlation spectroscopy (FCS) traces (λ_{ex} = 470 nm, λ_{em} = 532–800 nm) of PQACz-T (5 nM) in the form of PQNPs (red) and nanoparticles (f_w = 99%, green); the FCS data are fitted using Eqn. (3); inset: diffusion coefficients (D_t, $\mu m^2 \cdot s^{-1}$) and hydrodynamic radius (r_h, nm) of PQNPs and nanoaggregates (f_w = 99%), respectively. (d) Normalized absorption, emission, and excitation spectra of PQNPs in aqueous dispersion. (e) Transient PL decay curves at the microsecond timescale of PQNPs at room temperature under ambient conditions; inset: transient PL decay curves at the nanosecond timescale of PQNPs. (f) Laser power-dependent emission spectra of PQNPs under ambient conditions; inset: linear fitting of the emission intensity of the PQNPs as a function of excitation power.

cubated with the aqueous dispersion of PQNPs (125 µg/mL) for 15 minutes. A distinct punctate pattern was noticeable in the confocal laser scanning microscopy images, indicating the internalization of PQNPs in the LDs (SI, Figure S34). The intracellular localization of PQNPs was confirmed in live HeLa cells by the co-staining experiment with BODIPY 493/503 (commercial dye for staining of LDs, Figure 7a–c). The corresponding Pearson's coefficient of colocalization value of 0.96 indicated the LD specificity of the probe (Figure 7d).

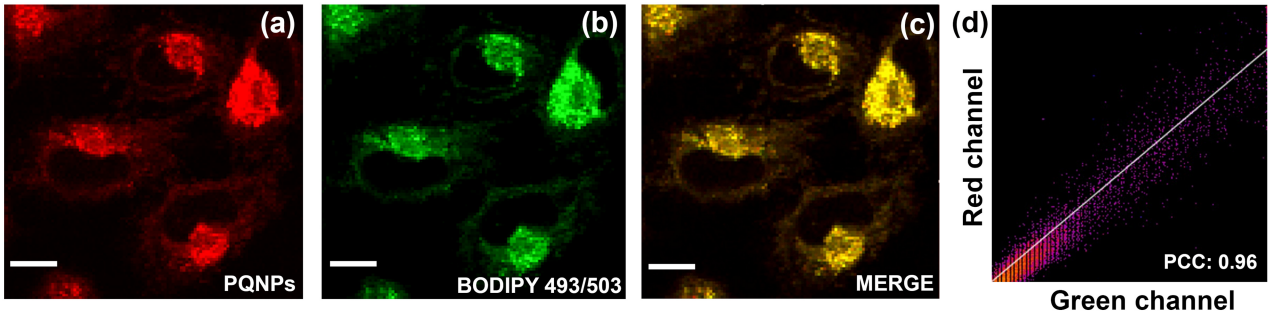

Figure 7 Confocal laser scanning microscopy (CLSM) colocalization images of HeLa cells incubated with (a) PQNPs (λ_{ex} = 470 nm, λ_{em} = 610–800 nm), (b) lipid droplet tracker dye, BODIPY 493/503 (λ_{ex} = 470 nm, λ_{em} = 510–530 nm), and (c) merged image. (d) Pearson's colocalization coefficient of red (PQNPs) and green (BODIPY 493/503) channels was found to be 0.96, indicating the lipid droplet staining by PQNPs. Scale (a–c) = 20 µm.

LDs are universal lipid-rich storage organelles consisting of hydrophobic neutral lipids with an outer phospholipid monolayer.[62,63] The inherent hydrophobic nature of PQACz-T (calculated log*P* = 19.4) was attributed to the LD specificity of PQNPs, which was unaffected by the influence of F-127 micelles (SI, Table S18).[64,65] Further, the colocalization experiments with MitoTracker Green and LysoTracker Green confirmed no specific staining of mitochondria and lysosome, respectively, by PQNPs (SI, Figure S35). PQNPs have longer fluorescence lifetimes in the order of microseconds than the short-lived autofluorescence or background fluorescence in the cellular environments (< 10 ns). The long-lived emissive characteristic in the aqueous medium suggests PQNPs as promising candidates for future applications in time-gated imaging.

Conclusions

In summary, we rationalized the variation of the excited-state properties due to the substitution of a *t*-butyl group in the donor carbazole moiety in multichromophoric D–A–D compounds, PQACz-T (with alkyl substitution) and PQCz-T (without alkyl substitution), having a rigid dibenzopyridoquinoxaline acceptor core. Both compounds exhibited TADF in the doped polymer films. PQACz-T was found to be self-assembled to molecular nanoaggregates of diverse size and shape in THF–water mixtures, presumably due to the hydrophobic interactions imparted by the *t*-butyl units. PQACz-T nanoaggregates exhibited bright red emission along with delayed fluorescence in the aqueous dispersion. Further, the smaller-sized, homogeneous distribution of fluorescent nanoparticles in water was fabricated upon encapsulating PQACz-T in a triblock copolymer, F-127 matrix, for intracellular imaging. Cytocompatible, polymer-encapsulated PQACz-T nanoparticles were employed for specific imaging of LDs in HeLa cells. The present study paves the way for further exploration of the molecular self-assembly processes of TADF nanoaggregates for specific intracellular sensing and imaging.

Experimental Section

Synthesis of 2,7-bis(3,6-di-*tert*-butyl-9H-carbazol-9-yl)dibenzo[*f*,*h*]pyrido[3,4-*b*]quinoxaline (PQACz-T): To a mixture of P3 (100 mg, 1 equiv.), 3,6 di-*t*-butylcarbazole (DTCz, 2.1 equiv.), $Pd_2(dba)_3$ (0.15 equiv.), *t*-BuOK (4 equiv.) and x-Phos (0.15 equiv.), 10 mL of toluene was added and stirred under an Ar atmosphere at 110 °C for 24 h. After cooling the reaction mixture to room temperature, the reaction was quenched by the addition of 10% aqueous $NaHCO_3$ and 20 mL distilled water. The organic layer was then extracted with dichloromethane (3 × 15 mL), dried over anhydrous $MgSO_4$, and concentrated under vacuum. The product was purified by column chromatography (neutral alumina, 10% DCM/hexane) to afford an orange solid with a yield of 65% (123 mg, Scheme S4, mp: 340 °C, based on the decomposition colour change).

^{1}H NMR (700 MHz, $CDCl_3$): δ 9.76 (s, 1 H), 9.69 (m, 2 H), 8.87 (m, 1 H), 8.81 (m, 2 H), 8.23 (s, 4 H), 8.11 (m, 3 H), 7.56 (m, 8 H), 1.52 (s, 36 H). ^{13}C NMR (126 MHz, $CDCl_3$): δ 155.44, 146.67, 145.83, 144.19, 143.70, 143.46, 139.13, 138.50, 137.18, 131.23, 129.79, 124.99, 124.58, 124.07, 123.83, 121.40, 116.53, 109.25, 34.85, 32.06. HRMS (APCI): calculated for $C_{59}H_{57}N_5$ $[M]^+$: 836.1400 g·mol^{-1}, found: 836.4711 g·mol^{-1}.

The detailed synthetic procedures and yields of the intermediate compounds are mentioned in the SI. The thin films were fabricated by spin-coating the toluene solution of 10 wt% of PQACz-T and PQCz-T in PMMA, followed by drying under vacuum. For the fabrication of nanoaggregates of the compounds, a stock solution of 1 mM was prepared in dry THF. 30 µL of the stock solution was rapidly added to the binary solvent mixture of THF–water (total volume: 3 mL) under sonication for 1 min. Polymer-encapsulated nanoparticles (PQNPs) for intracellular imaging were fabricated using a stock solution of PQACz-T (1 mg) and polyethylene–polypropylene glycol (Pluronic F-127, 12 mg) in $CHCl_3$ (1.1 mL). Subsequently, the evaporation of organic solvent resulted in a film, which was dispersed in distilled water. The aqueous dispersion upon filtration through a nanoporous membrane (0.2 µm) was used for further experiments.

Funding Information

DST-SERB (Project no. EMR/2017/000 233), Council of Scientific and Industrial Research (CSIR), New Delhi (No. 01 (2878)/17/EMR-II).

Acknowledgment

We thank the infrastructural support from Indian Institute of Science Education and Research Bhopal (IISERB), and the TEM facility at the Department of Chemistry, IISERB, supported through the DST FIST programme. S. D. and B. S. thank IISERB, and S. K. and M. S. thank University Grants Commission and Council of Scientific and Industrial Research for a fellowship, respectively. S. D. acknowledges Ms. Nitu Saha for help with the MTT assay and Ms. Ashima Negi and Dr. Ankur Gupta at IISERB for helping in the laser fluence-dependent study.

Supporting Information

Details of synthesis, characterization, absorption, emission and lifetime data of PQACz-T, time-resolved emission spectra, TADF characteristics, and self-assembly behaviour of PQACz-T and PQCz-T, supporting colocalization experiments with PQACz-T nanoparticles and the comparative analysis of lipid droplet imaging are given in the Supporting Information.

Supporting Information for this article is available online at https://doi.org/10.1055/a-1679-9558.

Conflict of Interest

The authors declare the following competing financial interest. A patent application has been filed on "Dibenzopyridoquinoxaline based derivatives" with A. Patra, B. Sk, M. Sarkar and S. Kundu as inventors.[66]

References

(1) Uoyama, H.; Goushi, K.; Shizu, K.; Nomura, H.; Adachi, C. *Nature* **2012**, *492*, 234.
(2) Tao, Y.; Yuan, K.; Chen, T.; Xu, P.; Li, H.; Chen, R.; Zheng, C.; Zhang, L.; Huang, W. *Adv. Mater.* **2014**, *26*, 7931.
(3) Liu, Y.; Li, C.; Ren, Z.; Yan, S.; Bryce, M. R. *Nat. Rev. Mater.* **2018**, *3*, 18020.
(4) Im, Y.; Kim, M.; Cho, Y. J.; Seo, J. A.; Yook, K. S.; Lee, J. Y. *Chem. Mater.* **2017**, *29*, 1946.
(5) Yang, Z.; Mao, Z.; Xie, Z.; Zhang, Y.; Liu, S.; Zhao, J.; Xu, J.; Chi, Z.; Aldred, M. P. *Chem. Soc. Rev.* **2017**, *46*, 915.
(6) Chen, X. K.; Kim, D.; Brédas, J. L. *Acc. Chem. Res.* **2018**, *51*, 2215.
(7) Pashazadeh, R.; Pander, P.; Bucinskas, A.; Skabara, P. J.; Dias, F. B.; Grazulevicius, J. V. *Chem. Commun.* **2018**, *54*, 13857.
(8) Zhu, Z.; Tian, D.; Gao, P.; Wang, K.; Li, Y.; Shu, X.; Zhu, J.; Zhao, Q. *J. Am. Chem. Soc.* **2018**, *140*, 17484.
(9) Paisley, N. R.; Halldorson, S. V.; Tran, M. V.; Gupta, R.; Kamal S.; Algar, R.; Hudson, Z. M. *Angew. Chem. Int. Ed.* **2021**, *60*, 18630.
(10) Kawasumi, K.; Wu, T.; Zhu, T.; Chae, H. S.; Voorhis, T. V.; Baldo, M. A.; Swager, T. M. *J. Am. Chem. Soc.* **2015**, *137*, 11908.
(11) Data, P.; Pander, P.; Okazaki, M.; Takeda, Y.; Minakata, S.; Monkman, A. P. *Angew. Chem. Int. Ed.* **2016**, *55*, 5739.
(12) Kuila, S.; Garain, S.; Banappanavar, G.; Garain, B. C.; Kabra, D.; Pati, S. K.; George, S. *J. Phys. Chem. B* **2021**, *125*, 4520.
(13) Imagawa, T.; Hirata, S.; Totani, K.; Watanabe, T.; Vacha, M. *Chem. Commun.* **2015**, *51*, 13268.
(14) Ward, J. S.; Nobuyasu, R. S.; Batsanov, A. S.; Data, P.; Monkman, A. P.; Dias, F. B.; Bryce, M. R. *Chem. Commun.* **2016**, *52*, 2612.
(15) Klimash, A.; Pander, P.; Klooster, W. T.; Coles, S. J.; Data, P.; Dias, F. B.; Skabara, P. J. *J. Mater. Chem. C* **2018**, *6*, 10557.
(16) Santos, P. L.; Chen, D.; Rajamalli, P.; Matulaitis, T.; Cordes, D. B.; Slawin, A. M. Z.; Jacquemin, D.; Colman, E. Z.; Samuel, I. D. W. *ACS Appl. Mater. Interfaces* **2019**, *11*, 45171.
(17) Xie, F. M.; Li, H. Z.; Dai, G. L.; Li, Y. Q.; Cheng, T.; Xie, M.; Tang, J. X.; Zhao, X. *ACS Appl. Mater. Interfaces* **2019**, *11*, 26144.
(18) Sk, B.; Sharma, S.; James, A.; Kundu, S.; Patra, A. *J. Mater. Chem. C* **2020**, *8*, 12943.
(19) Voll, C. C. A.; Markopoulos, G.; Wu, T. C.; Welborn, M.; Engelhart, J. U.; Rochat, S.; Han, G. G. D.; Sazama, G. T.; Lin, T. A.; Voorhis, T. V.; Baldo, M. A.; Swager, T. M. *Org. Mater.* **2020**, *2*, 1.
(20) Xiao, Y. F.; Chen, J. X.; Li, S; Tao, W. W.; Tian, S.; Wang, K.; Cui, X.; Huang, Z.; Zhang, X. H.; Lee, C. S. *Chem. Sci.* **2020**, *11*, 888.
(21) Wang, S.; Cheng, Z.; Song, X.; Yan, X.; Ye, K.; Liu, Y.; Yang, G.; Wang, Y. *ACS Appl. Mater. Interfaces* **2017**, *9*, 9892.
(22) Wei, W.; Yang, Z.; Chen, X.; Liu, T.; Mao, Z.; Zhao, J.; Chi, Z. *J. Mater. Chem. C* **2020**, *8*, 3663.
(23) Bhattacharjee, I.; Acharya, N.; Bhatia, H.; Ray, D. *J. Phys. Chem. Lett.* **2018**, *9*, 2733.
(24) Li, C.; Duan, R.; Liang, B.; Han, G.; Wang, S.; Ye, K.; Liu, Y.; Yi, Y.; Wang, Y. *Angew. Chem. Int. Ed.* **2017**, *56*, 11525.
(25) Hu, W.; Guo, L.; Bai, L.; Miao, X.; Ni, Y.; Wang, Q.; Zhao, H.; Xie, M.; Li, L.; Lu, X.; Huang, W.; Fan, Q. *Adv. Healthcare Mater.* **2018**, *7*, 1800299.
(26) Zhang, Y. L.; Ran, Q.; Wang, Q.; Liu, Y.; Hänish, C.; Reineke, S.; Fan, J.; Liao, L. S. *Adv. Mater.* **2019**, *31*, 1902368.
(27) Ni, F.; Zhu, Z.; Tong, X.; Zeng, W.; An, K.; Wei, D.; Gong, S.; Zhao, Q.; Zhou, X.; Yang, C. *Adv. Sci.* **2019**, *6*, 1801729.
(28) Jena, S.; Dhanalakshmi, P.; Bano, G.; Thilagar, P. *J. Phys. Chem. B* **2020**, *124*, 5393.
(29) Englman, R.; Jortner, J. *Mol. Phys.* **1970**, *18*, 145.
(30) Srujana, P.; Sudhakar, P.; Radhakrishnan, T. P. *J. Mater. Chem. C* **2018**, *6*, 9314.
(31) Chen, Y.; Lam, J. W. Y.; Kwok, R. T. K.; Liu, B.; Tang, B. Z. *Mater. Horiz.* **2019**, *6*, 428.
(32) Kim, J. H.; Yun, J. H.; Lee, J. Y. *Adv. Opt. Mater.* **2018**, *6*, 1800255.
(33) Kuila, S.; Ghorai, A.; Samanta, P. K.; Siram, R. B. K.; Pati, S. K.; Narayan, K. S.; George, S. *Chem. Eur. J.* **2019**, *25*, 16007.
(34) Lin, M. J.; Jiménez, Á. J.; Burschka, C.; Würthner, F. *Chem. Commun.* **2012**, *48*, 12050.
(35) Fan, Y.; Li, Q.; Li, Z. *Mater. Chem. Front.* **2021**, *5*, 1525.
(36) Gong, Y.; Zhang, Y.; Yuan, W. Z.; Sun, J. Z.; Zhang, Y. *J. Phys. Chem. C* **2014**, *118*, 10998.
(37) Sk, B.; Khodia, S.; Patra, A. *Chem. Commun.* **2018**, *54*, 1786.
(38) Zheng, X.; Zhu, W.; Ni, F.; Ai, H.; Gong, S.; Zhou, X.; Sessler, J. L.; Yang, C. *Chem. Sci.* **2019**, *10*, 2342.
(39) Singha, S.; Kim, D.; Roy, B.; Sambasivan, S.; Moon, H.; Rao, A. S.; Kim, J. Y.; Joo, T.; Park, J. W.; Rhee, Y, M.; Wang, T.; Kim, K. H.; Shin, Y, H.; Jung, J.; Ahn, K. H. *Chem. Sci.* **2015**, *6*, 4335.
(40) Sasaki, S.; Drumen, G. P. C.; Konishi, G. *J. Mater. Chem. C* **2016**, *4*, 2731.
(41) Reja, S. I.; Khan, I. A.; Bhalla, V.; Kumar, M. *Chem. Commun.* **2016**, *52*, 1182.
(42) Abdel-Shafi, A. A.; Worrall, D. R. *J. Photochem. Photobiol., A.* **2005**, *172*, 170.
(43) Cheng, Y. H.; Belyaev, A.; Ho, M. L.; Koshevoy, I. O.; Chou, P. T. *Phys. Chem. Chem. Phys.* **2020**, *22*, 27144.
(44) Zhang, D.; Cai, M.; Zhang, Y.; Zhang, D.; Duan, L. *Mater. Horiz.* **2016**, *3*, 145.
(45) Pommerehne, J.; Vestweber, H.; Guss, W.; Mahrt, R. F.; Bässler, H.; Porsch, M.; Daub, J. *Adv. Mater.* **1995**, *7*, 551.
(46) Kim, H. S.; Park, S. R.; Suh, M. C. *J. Phys. Chem. C* **2017**, *121*, 13986.
(47) Lin, J. A.; Li, S. W.; Liu, Z. Y.; Chen, D. G.; Huang, C. Y.; Wei, Y. C.; Chen, Y. Y.; Tsai, Z. H.; Lo, C. Y.; Hung, W. Y.; Wong, K. T.; Chou, P. T. *Chem. Mater.* **2019**, *31*, 5981.
(48) Guo, J.; Fan, J.; Lin, L.; Zeng, J.; Liu, H.; Wang, C. K.; Zhao, Z.; Tang, B. Z. *Adv. Sci.* **2019**, *6*, 1801629.
(49) Qi, S.; Kim, S.; Nguyen, V. N.; Kim, Y.; Niu, G.; Kim, G.; Kim, S. J.; Park, S.; Yoon, J. *ACS Appl. Mater. Interfaces* **2020**, *12*, 51293.

(50) Tsuchiya, Y.; Ikesue, K.; Nakanotani, H.; Adachi, C. *Chem. Commun.* **2019**, *55*, 5215.
(51) Li, X.; Baryshnikov, G.; Ding, L.; Bao, X.; Li, X.; Lu, J.; Liu, M.; Shen, S.; Luo, M.; Zhang, M.; Ågren, H.; Wang, X.; Zhu, L. *Angew. Chem. Int. Ed.* **2020**, *59*, 7548.
(52) Qin, W.; Feng, G.; Li, M.; Yang, Z.; Liu, B.; Tang, B. Z. *Adv. Funct. Mater.* **2014**, *24*, 635.
(53) Zhang, K.; Zhang, Y.; Ma, Y.; Fan, J.; Wang, C. K.; Lin, L. *J. Phys. Chem. A* **2020**, *124*, 8540.
(54) Zhang, H.; Chen, P. Z.; Niu, L. Y.; Yang, Q. Z. *Mater. Chem. Front.* **2020**, *4*, 285.
(55) Li, N.; Liu, Y. Y.; Li, Y.; Zhuang, J. B.; Cui, R. R.; Gong, Q.; Zhao, N.; Tang, B. Z. *ACS Appl. Mater. Interfaces* **2018**, *10*, 24249.
(56) Kundu, S.; Chowdhury, A.; Nandi, S.; Bhattacharyya, K.; Patra, A. *Chem. Sci.* **2021**, *12*, 5874.
(57) Middha, E.; Liu, B. *ACS Nano* **2020**, *14*, 9228.
(58) Cheng, H. B.; Li, Y.; Tang, B. Z.; Yoon, J. *Chem. Soc. Rev.* **2020**, *49*, 21.
(59) Chen, C.; Wylie, R. A. L.; Klinger, D.; Connal, L. A. *Chem. Mater.* **2017**, *29*, 1918.
(60) Qi, J.; Sun, C.; Zebibula, A.; Zhang, H.; Kwok, R. T. K.; Zhao, X.; Xi, W.; Lam, J. W. Y.; Qian, J.; Tang, B. Z. *Adv. Mater.* **2018**, *30*, 1706856.
(61) Dong, C.; Irudayaraj, J. *J. Phys. Chem. B* **2012**, *116*, 12125.
(62) Martin, S.; Parton, R. G. *Nat. Rev. Mol. Cell Biol.* **2006**, *7*, 373.
(63) Sk, B.; Thakre, P. K.; Tomar, R. S.; Patra, A. *Chem. Asian J.* **2017**, *12*, 2501.
(64) Rakshit, S.; Das, S.; Govindaraj, V.; Maini, R.; Kumar, A.; Datta, A. *J. Phys. Chem. B* **2020**, *124*, 10282.
(65) Guo, X.; Tang, B.; Wu, H.; Wu, Q.; Xie, Z.; Yu, C.; Hao, E.; Jiao, L. *Mater. Chem. Front.* **2021**, *5*, 3664.
(66) Patra, A.; Sk, B.; Sarkar, M.; Kundu, S. Indian Pat. Appl. 201921041228, October 11, 2019.